

# RSC Advances



This is an *Accepted Manuscript*, which has been through the Royal Society of Chemistry peer review process and has been accepted for publication.

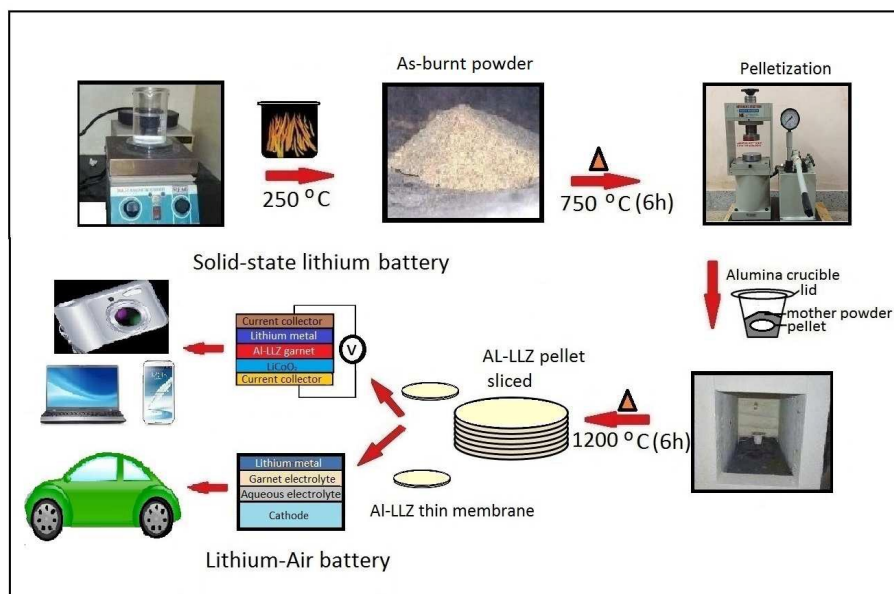
*Accepted Manuscripts* are published online shortly after acceptance, before technical editing, formatting and proof reading. Using this free service, authors can make their results available to the community, in citable form, before we publish the edited article. This *Accepted Manuscript* will be replaced by the edited, formatted and paginated article as soon as this is available.

You can find more information about *Accepted Manuscripts* in the [Information for Authors](#).

Please note that technical editing may introduce minor changes to the text and/or graphics, which may alter content. The journal's standard [Terms & Conditions](#) and the [Ethical guidelines](#) still apply. In no event shall the Royal Society of Chemistry be held responsible for any errors or omissions in this *Accepted Manuscript* or any consequences arising from the use of any information it contains.

## Table of Content

A facile combustion method was developed for the rapid synthesis of large volume of high  $\text{Li}^+$  conductive cubic phase  $\text{Li}_{6.28}\text{Al}_{0.24}\text{La}_3\text{Zr}_2\text{O}_{12}$  with uniform particle size at the nanometer level for industrial production of solid electrolyte for the fabrication of rechargeable all-solid-state lithium and Li-air battery.



## Facile synthesis of high lithium ion conductive cubic phase lithium garnets for electrochemical energy storage devices

L. Dhivya, K. Karthik, S. Ramakumar and Ramaswamy Murugan\*

Department of Physics, Pondicherry University, Puducherry - 605 014, India.

\*Email: moranamurugan.phy@pondiuni.edu.in

### Abstract

$\text{Li}_7\text{La}_3\text{Zr}_2\text{O}_{12}$  (LLZ) lithium garnet is a prospective solid electrolyte for all-solid-state lithium batteries and Li-Air batteries due to its high room temperature  $\text{Li}^+$  conductivity ( $10^{-4} \text{ Scm}^{-1}$ ) and chemical stability against lithium metal and few aqueous solutions. Preparation of cubic phase ( $Ia\bar{3}d$ ) LLZ by solid state synthesis technique requires repeated heat treatments along with the intermittent grinding and long duration of sintering. However for industrial production, low cost, scalable and fast synthetic techniques are essential. In this work, LLZ and  $\text{Li}_{6.28}\text{Al}_{0.24}\text{La}_3\text{Zr}_2\text{O}_{12}$  (Al-LLZ) lithium garnets were successfully prepared in shorter duration of time by simple combustion technique and also the effect of the excess lithium source on structure,  $\text{Li}^+$  conductivity and morphology of the synthesized materials were investigated. Powder X-ray diffraction (PXRD) and Raman spectra of as-burnt powder sintered at  $950^\circ\text{C}$  revealed tetragonal phase ( $I4_1/acd$ ) for LLZ whereas high conductive cubic phase ( $Ia\bar{3}d$ ) for Al-LLZ. Among all the prepared samples, Al-LLZ with 10 wt % excess lithium source sintered at  $1200^\circ\text{C}$  for just 6 h exhibits a maximized relative density of 95% and total (bulk + grain-boundary)  $\text{Li}^+$  conductivity of  $5.1 \times 10^{-4} \text{ Scm}^{-1}$  at  $30^\circ\text{C}$  with particle size of around 613 nm.

## Introduction

Recent investigations indicated that garnet structured high  $\text{Li}^+$  conductive cubic phase ( $Ia\bar{3}d$ )  $\text{Li}_7\text{La}_3\text{Zr}_2\text{O}_{12}$  (LLZ) ceramic solid electrolyte may be suitable for the fabrication of high energy density all-solid-state lithium battery and Li-air batteries due to its high  $\text{Li}^+$  conductivity and satisfactory electrochemical stability against potential electrodes, lithium metal and few aqueous solutions.<sup>1-7</sup>

High  $\text{Li}^+$  conductive cubic phase LLZ can be obtained by different synthesis methods, such as solid-state reactions from mixtures of carbonate, oxide, nitrates and hydroxide<sup>2,3, 8-10</sup>, sol-gel method<sup>11</sup>, Pechini<sup>12</sup>, spray pyrolysis<sup>13</sup> and organic chemical vapour deposition techniques<sup>14</sup>. In the reported work to date, the solid-state reaction is the most commonly used method to synthesize LLZ. In the solid-state synthesis, high reaction temperature around 1230 °C, long duration of sintering of 36 h in alumina crucible along with intermittent grinding and repeated heat treatment is necessary to obtain dense and highly conductive cubic ( $Ia\bar{3}d$ ) phase LLZ rather than the low  $\text{Li}^+$  conductive tetragonal ( $I4_1/acd$ ) phase LLZ.<sup>2,3,8</sup> It has been proved that the unintentional inclusion of  $\text{Al}^{3+}$  from the alumina crucibles into the LLZ pellet during the high-temperature sintering helps to stabilize the high  $\text{Li}^+$  conductive cubic phase.<sup>14-16</sup> The incorporation of Al in LLZ serves two purposes: (1) stabilize the cubic phase<sup>15,16</sup> and/or (2) act as a sintering aid to enhance the density.<sup>17</sup> The optimized content of Li and Al required for high  $\text{Li}^+$  conductive cubic phase LLZ ( $Ia\bar{3}d$ ) was 6.24 moles and 0.24 moles, respectively.<sup>17</sup>

In addition to heat treatment and doping strategy, the amount of excess lithium salt in starting materials may be another important factor in determining the density of high  $\text{Li}^+$  conductive cubic phase LLZ. Through solid-state reaction technique it is difficult to control the chemical stoichiometry of the lithium garnets owing to lithium loss at high sintering temperature.

Efforts were made to overcome the difficulties encountered in solid-state reaction technique by switching over to wet chemical techniques.<sup>7, 11, 18-20</sup>

In the present work, we have focused on relatively simple and cost effective solution combustion technique for the rapid synthesis of high  $\text{Li}^+$  conductive cubic phase nanosized  $\text{Li}_7\text{La}_3\text{Zr}_2\text{O}_{12}$  (LLZ) and Al doped  $\text{Li}_7\text{La}_3\text{Zr}_2\text{O}_{12}$ , i.e.,  $\text{Li}_{6.28}\text{Al}_{0.24}\text{La}_3\text{Zr}_2\text{O}_{12}$  (Al-LLZ). The phase evolution of the samples with different heat treatment temperatures was investigated. Also the effect of addition of excess amount of lithium reactants on the structure,  $\text{Li}^+$  conductivity and morphology of the synthesized materials was examined.

## Experimental

### Synthesis of LLZ and Al doped LLZ

Appropriate amount of  $\text{LiNO}_3$  (0, 10 and 20 wt.% excess was added to avoid the expected loss of lithium) (Sigma-Aldrich),  $\text{La}(\text{NO}_3)_3 \cdot 6\text{H}_2\text{O}$  (Sigma-Aldrich),  $\text{ZrO}(\text{NO}_3)_2 \cdot 5\text{H}_2\text{O}$  (Sigma-Aldrich) and glycine [ $\text{CH}_2\text{NH}_2\text{COOH}$ ] (Sigma-Aldrich) ) with 99.9% purity were used as reactants for the preparation of  $\text{Li}_7\text{La}_3\text{Zr}_2\text{O}_{12}$  (LLZ) and additionally appropriate amount of  $\text{Al}(\text{NO}_3)_3 \cdot 9\text{H}_2\text{O}$  was added for the preparation of Al doped  $\text{Li}_7\text{La}_3\text{Zr}_2\text{O}_{12}$ , i.e.,  $\text{Li}_{6.28}\text{Al}_{0.24}\text{La}_3\text{Zr}_2\text{O}_{12}$  (Al-LLZ) by combustion technique. The molar ratio of metal nitrates to glycine was experimented with various ratio and the optimized ratio was found to be 1:1. The metal nitrates and glycine were dissolved together in a minimum amount of distilled water to get a transparent solution. The solution was placed on the hot plate with continuous stirring at  $90^\circ\text{C}$  for 30 mins. After the evaporation of the solvent, a very viscous brown gel was formed. When finally all water molecules were removed from the mixture the temperature of the hot plate was increased in stepwise to  $250^\circ\text{C}$  then the viscous gel began frothing. After few minutes, the gel automatically ignited and burnt with glowing flints to produce voluminous powder. The obtained

powder was sintered at 750 °C for 6 h for further investigation. The powder sintered at 750 °C for 6 h was ground well and pressed into pellets. The pellets were covered with the mother powder to reduce possible lithium loss and sintered at 950 °C for 24 h and 1200 °C for 6 h in a closed alumina crucible. All the investigated samples were prepared in open air atmosphere and sintered using a muffle furnace with air atmosphere. After the sintering process the samples were allowed to undergo natural furnace cooling with air atmosphere. The LLZ lithium garnet prepared without excess lithium source, with 10 wt.% and 20 wt.% excess lithium source will be hereafter referred as, respectively, LLZ-0, LLZ-10 and LLZ-20 and similarly the Al-LLZ prepared without excess lithium source, with 10 wt.% and 20 wt.% excess lithium source will be referred as, respectively, Al-LLZ-0, Al-LLZ-10 and Al-LLZ-20.

### Characterization

Thermal analysis (thermogravimetric/differential scanning calorimetric analysis (TG/DSC)) was performed with a SDT Q600 (TA) under air flow with a heating rate of 20 °C/min in the temperature range from room temperature to 1000 °C.

The sintered pellets were crushed into powder form for powder X-ray diffraction (PXRD) and Raman measurements. The crystal structure and phase purity of the prepared samples were examined by powder X-ray diffraction (PXRD) using X'pert PRO PANalytical X-ray diffractometer with Cu-K $\alpha$  radiation of  $\lambda = 1.5418 \text{ \AA}$  from  $2\theta = 10^\circ$  to  $80^\circ$  with a step width of  $0.025^\circ$ .

Confocal micro-Raman spectra have been recorded at room temperature in the range 50-4000  $\text{cm}^{-1}$  using a Renishaw in via Reflex spectrometer with a 50 mW internal Ar<sup>+</sup> laser source of excitation wavelength 514 nm. HITACHI S-3400N scanning electron microscope (SEM) equipped with energy dispersive X-ray detector (EDX) was used to examine the morphology of

the prepared samples. The particle-size distribution of the synthesized powders was determined by a laser-diffraction particle size analyser Malvern Mastersizer 2000. The relative densities of the sintered pellets at room temperature were obtained with the Archimedes' principle using deionised water as the immersion medium.

Electrical conductivity measurements were performed using  $\text{Li}^+$  blocking Au-electrodes (Au paste cured at 600 °C for 1 h) in the frequency range 20 Hz to 15 MHz using a Wayne Kerr 6500B precision impedance analyzer in the temperature range from 30 °C to 200 °C. The PXRD, Raman and electrical conductivity measurements were carried out in open air atmosphere.

## Results and discussion

### Thermal analysis

The TG and DSC curves for as-burnt LLZ and Al-LLZ obtained without excess lithium source, with 10 wt.% and 20 wt.% excess lithium source, are shown as Figs. 1(a) and (b), respectively. In general three major steps of weight losses were observed in the TG thermograms. An initial weight loss observed below 100 °C in TG (Fig. 1(a)) and the corresponding endotherms observed at around 100 °C in DSC (Fig. 1(b)) might correspond to the elimination of adsorbed water molecules. The second weight loss observed in the temperature range from 250 °C to 625 °C might be due to the decomposition of the residual organic fuel and nitrates ( $\text{NO}_3^-$ ) ions present in the sample. The onset of third stage of weight loss was observed around 700 °C. However the completion of last stage of weight loss varies for the samples. The last step weight loss may arise from the removal of the residual carbon. The TG thermograms as shown in Fig. 1(a) indicated the completion of the reaction and formation of possible lithium garnet phase occurs relatively at low sintering temperature for Al-LLZ compared to that of LLZ. In the case of LLZ-20 the decomposition process appears to be not yet completed even at 1000 °C.

### Powder X-ray diffraction (PXRD)

The PXRD patterns of LLZ-0, LLZ-10 and LLZ-20 sintered at various temperatures are shown as Figs. 2(a) - (c), respectively, along with the reported patterns of high  $\text{Li}^+$  conductive cubic and tetragonal phase LLZ.<sup>21</sup> The major difference between the tetragonal phase LLZ and high  $\text{Li}^+$  conductive cubic are the presence of characteristic doublets ( $2\theta=30.5^\circ$ ) for the tetragonal phase and sharp diffraction peaks in the case of high  $\text{Li}^+$  conductive cubic phase. The other major difference is the presence of three peaks in the case of high  $\text{Li}^+$  conductive cubic phase and six peaks in the case of tetragonal phase LLZ in the  $2\theta$  range  $50-55^\circ$ . The low temperature cubic LLZ exhibit shift in the diffraction peaks towards the lower diffraction i.e., increase in the cubic lattice constant due to the replacement of Li-O bonds by O-H $\cdots$ O hydrogen bonds through  $\text{Li}^+/\text{H}^+$  exchange.<sup>22</sup> The PXRD patterns of as-burnt LLZ-0, LLZ-10 and LLZ-20 shown in Figs. 2(a) - (c) indicated that the pyrochlore  $\text{La}_2\text{Zr}_2\text{O}_7$  (JCPDS No. 73-444) is the first major crystallographic phase formed for all the samples along with minor  $\text{La}_2\text{O}_3$  phase. The reaction pathway for the formation of LLZ in this work appears to be similar to that observed in the Pechini<sup>12,19</sup> and sol-gel method,<sup>11,18</sup> where  $\text{La}_2\text{Zr}_2\text{O}_7$  pyrochlore is the first crystallographic phase formed at the lower temperature upon heating.

The PXRD pattern of LLZ-0 sintered at  $750^\circ\text{C}$  exhibit mixed tetragonal phase LLZ and  $\text{La}_2\text{Zr}_2\text{O}_7$  pyrochlore phase (Fig. 2(a)). The PXRD pattern of LLZ-0 sintered at  $950^\circ\text{C}$  exhibit tetragonal phase LLZ as major phase along with the pyrochlore  $\text{La}_2\text{Zr}_2\text{O}_7$  as minor phase. When the sintering temperature was increased to  $1200^\circ\text{C}$ , the  $\text{La}_2\text{Zr}_2\text{O}_7$  phase disappeared. The presence of broad diffraction peaks in the PXRD pattern of LLZ-0 sintered at  $1200^\circ\text{C}$  shown as Fig. 2(a) indicated the possible mixed tetragonal and cubic-like phases.

The PXRD pattern of LLZ-10 sintered at 750 °C exhibit mixed tetragonal phase LLZ along with the pyrochlore  $\text{La}_2\text{Zr}_2\text{O}_7$  (Fig. 2(b)). When the sintering temperature was further increased to 950 °C, the  $\text{La}_2\text{Zr}_2\text{O}_7$  phase reacts with the residual lithium and lanthanum oxides to form the single phase tetragonal LLZ as shown in Fig. 2(b). The tetragonal phase can be recognized by doublet peak; the most prominent is centered at  $2\theta=30.5^\circ$ . At the sintering temperature of 1200 °C (Fig. 2(b)), the characteristic tetragonal phase peak doublets merges into single peak results into cubic-like LLZ.

The PXRD pattern of LLZ-20 sintered at 750 °C indicates the characteristic splitting of diffraction peak at  $2\theta=30.5^\circ$ , which confirms the formation of tetragonal phase LLZ as shown in Fig. 2(c). Further increase in the sintering temperature to 950 °C the PXRD pattern revealed the presence of tetragonal phase LLZ as major phase along with minor  $\text{Li}_4\text{ZrO}_4$  secondary phase. Xie et al. reported that lithium deficiency leads in to  $\text{La}_2\text{Zr}_2\text{O}_7$ , while excess lithium (50 wt.%) produce  $\text{Li}_2\text{ZrO}_3$  as secondary phases during the synthesis of LLZ.<sup>23</sup> When the sintering temperature increased to 1200 °C, the  $\text{Li}_4\text{ZrO}_4$  secondary phase disappeared and cubic-like LLZ with minor  $\text{La}_2\text{O}_3$  were appeared (Fig. 2(c)) as the final product of the synthesis.

The PXRD patterns of Al-LLZ-0, Al-LLZ-10 and Al-LLZ-20 sintered at various temperatures are shown as Figs. 3(a) - (c), respectively, along with the reported patterns of high  $\text{Li}^+$  conductive cubic and tetragonal phase LLZ.<sup>21</sup> The PXRD patterns of as-burnt Al-LLZ-0, Al-LLZ-10 and Al-LLZ-20 shown in Figs. 3(a) - (c), respectively, exhibited the formation of pyrochlore  $\text{La}_2\text{Zr}_2\text{O}_7$  (JCPDS No. 73-444) as the major phase along with few minor  $\text{La}_2\text{O}_3$  phase. The PXRD pattern of Al-LLZ-0 (Fig. 3(a)) sintered at 750 °C exhibit mixed cubic-like phase, pyrochlore  $\text{La}_2\text{Zr}_2\text{O}_7$  and  $\text{LaAlO}_3$ . The PXRD pattern of Al-LLZ-0 sintered at 950 °C indicates the presence of high  $\text{Li}^+$  conductive cubic phase LLZ as major phase. Moreover, the intensity of

the diffraction peaks of secondary phases of  $\text{La}_2\text{Zr}_2\text{O}_7$  and  $\text{LaAlO}_3$  were found to be decreased. The PXRD pattern of Al-LLZ-0 sintered at 1200 °C shown as Fig. 3(a) revealed that it was similar to the reported high  $\text{Li}^+$  conductive cubic phase LLZ.<sup>21</sup>

PXRD pattern of Al-LLZ-10 and Al-LLZ-20 sintered at 750 °C exhibit cubic-like LLZ and pyrochlore  $\text{La}_2\text{Zr}_2\text{O}_7$  as mixed phases along with  $\text{LaAlO}_3$  as minor phase. The PXRD pattern of Al-LLZ-10 and Al-LLZ-20 sintered at 950 °C confirm the high  $\text{Li}^+$  conductive cubic phase LLZ as major phase along with very minor  $\text{La}_2\text{Li}_{0.5}\text{Al}_{0.5}\text{O}_4$  impurity phase. The presence of sharp diffraction peaks corresponding only to that of the high  $\text{Li}^+$  conductive cubic phase in the PXRD pattern of Al-LLZ-10 sintered at 1200 °C (Fig. 3(b)) revealed the formation of well crystallized single phase high  $\text{Li}^+$  conductive cubic phase LLZ.<sup>21</sup> However, the PXRD pattern of Al-LLZ-20 sintered at 1200 °C (Fig. 3(c)) exhibit relatively broad diffraction peaks compared to that of Al-LLZ-10. The PXRD data confirmed that the addition of 0.24 moles of Al to LLZ promotes the modification of tetragonal phase LLZ to the high  $\text{Li}^+$  conductive cubic phase LLZ relatively at lower sintering temperature.

The PXRD patterns shown as Fig 2(a)-(c) and Fig 3 (a)-(c) are in agreement with the TG and DSC curves (Fig. 1(a), (b) and Fig.S1 in ESI†). The peak temperatures and enthalpies of endothermic peaks in DSC thermograms observed in the temperature range from 500 °C to 950 °C (See Fig. S1 in ESI†) increase with the increase of excess lithium source. The endotherms observed around 700 °C in DSC thermograms might be due to the reaction of  $\text{La}_2\text{Zr}_2\text{O}_7$  pyrochlore with the left over lithium and lanthanum oxides (Li-La-O) in the case of LLZ (as evidenced from Fig. 2(a)-(c)) and with lithium, lanthanum and aluminium oxide (Li-La-Al-O) in the case of Al-LLZ (as evidenced from Fig. 3(a)-(c)).

## Raman spectroscopic analysis

Raman scattering is a very powerful technique for identifying the phases of LLZ compared to PXRD technique. Earlier Raman studies on LLZ predicted that the vibration of heavy La cation between  $100\text{ cm}^{-1}$  and  $150\text{ cm}^{-1}$  and the Zr-O bond stretching observed around  $640\text{ cm}^{-1}$ .<sup>10</sup> For several lithium metal oxide materials it has been demonstrated that, the internal modes of  $\text{LiO}_6$  appear in the range  $200\text{-}300\text{ cm}^{-1}$ , whereas the internal modes of  $\text{LiO}_4$  occurs in the range  $350\text{-}500\text{ cm}^{-1}$ .<sup>24,25</sup>

The Raman spectra of tetragonal phase ( $I4_1/acd$ ) LLZ, high  $\text{Li}^+$  conductive cubic phase ( $Ia\bar{3}d$ ) and low temperature cubic phase LLZ<sup>20,21</sup> in the range  $75\text{-}800\text{ cm}^{-1}$  are shown as Fig. 4(a) - (c), respectively. The characteristic's Raman spectrum of tetragonal ( $I4_1/acd$ ) phase LLZ (Fig. 4(a)) consist of relatively larger number of Raman modes in the region  $200$  to  $500\text{ cm}^{-1}$  due to the ordered arrangements of lithium on tetrahedral  $8a$  site and octahedral  $16f$  and  $32g$  sites. The characteristic Raman modes for the tetragonal ( $I4_1/acd$ ) phase LLZ are the weak intense band at  $209\text{ cm}^{-1}$ , strong peak at  $248\text{ cm}^{-1}$ , medium intense peak at  $291\text{ cm}^{-1}$ , strong intense peaks at  $346, 370, 404\text{ cm}^{-1}$ , strong intense band at  $646\text{ cm}^{-1}$  and doublets at  $108$  and  $123\text{ cm}^{-1}$  as shown in Fig. 4(a).

The Raman spectrum of high  $\text{Li}^+$  conductive cubic ( $Ia\bar{3}d$ ) phase LLZ as shown in Fig. 4(b) exhibits few broad and fairly overlapping bands in the region  $200\text{-}500\text{ cm}^{-1}$  which might be due to the disordered highly mobile  $\text{Li}^+$  compared to the ordered  $\text{Li}^+$  in tetragonal phase.<sup>21</sup> The shoulder broad band at  $211\text{ cm}^{-1}$ , medium intense broad band at  $263\text{ cm}^{-1}$ , medium strong broad band at  $366\text{ cm}^{-1}$ , medium broad shoulder at  $417\text{ cm}^{-1}$ , strong intense band at  $645\text{ cm}^{-1}$ , medium intense peak at  $122\text{ cm}^{-1}$  and shoulder band at  $108\text{ cm}^{-1}$  are the characteristic Raman modes observed for the high  $\text{Li}^+$  conductive cubic phase ( $Ia\bar{3}d$ ) LLZ. The Raman spectrum in the  $200\text{-}$

500  $\text{cm}^{-1}$  region of high temperature cubic ( $Ia\bar{3}d$ ) phase LLZ exhibits broad bands associated to degenerate Raman modes, which turn out partly split in tetragonal LLZ phase because of its lower symmetry. In disordered system, the modifications in crystals local symmetry preventing atoms from vibrating in phase and leads to shift in the vibrational modes accompanied by broadening.

The Raman bands observed in the range 200-500  $\text{cm}^{-1}$  (Fig. 4(b) and (c)) corresponding to the expected internal modes of  $\text{LiO}_4$  and  $\text{LiO}_6$  clearly revealed the major difference between the high  $\text{Li}^+$  conductive cubic phase and low temperature cubic LLZ. The Raman spectrum of the low temperature cubic phase LLZ shown as Fig. 4(c) revealed strong intense peak at around 307 and 668  $\text{cm}^{-1}$ , medium intense bands at around 120, 184, 263, 344 and 380  $\text{cm}^{-1}$  and a weak bands at around 487 and 534  $\text{cm}^{-1}$ . The presence of relatively larger number of Raman modes in the region 200 to 500  $\text{cm}^{-1}$  for the low temperature cubic phase LLZ might be due to the relatively more ordered arrangements of lithium in the crystal lattice. In addition to the above difference an appreciable shift in the positions of vibrational stretching mode of  $\text{ZrO}_6$  octahedral units is observed. The shift of approximately 23  $\text{cm}^{-1}$  towards higher wave number for the Zr-O stretching mode and sharpening of the Raman bands in the region of internal modes of  $\text{LiO}_4$  and  $\text{LiO}_6$  for the low temperature cubic phase as shown in Fig. 4(c) revealed an appreciable modification in the crystal structure of the low temperature cubic and high  $\text{Li}^+$  conductive cubic phase LLZ. The cubic phase formed at low temperature might be due to the protonation in the course of the  $\text{Li}^+/\text{H}^+$  exchange mechanism.

The Raman spectra of LLZ-0, LLZ-10 and LLZ-20 sintered at various temperatures along with the reported high  $\text{Li}^+$  conductive cubic and tetragonal phase LLZ<sup>21</sup> in the range 50-1200  $\text{cm}^{-1}$  are shown as Figs. 5(a) - (c), respectively. Raman spectra of as-burnt LLZ-0, LLZ-10 and

LLZ-20 shown as Fig. 5(a) - (c), respectively, indicated the formation of pyrochlore  $\text{La}_2\text{Zr}_2\text{O}_7$  phase as revealed by the PXRD investigation. Raman spectrum of  $\text{La}_2\text{Zr}_2\text{O}_7$  phase shown as Fig. 5 (a) exhibits at least four major Raman modes at around 299, 394, 492  $\text{cm}^{-1}$  and 514  $\text{cm}^{-1}$ , which is similar to the reported data.<sup>20</sup>

Raman spectrum of LLZ-0 sintered at 750 °C exhibit the formation of tetragonal phase LLZ along with the pyrochlore  $\text{La}_2\text{Zr}_2\text{O}_7$  phase as shown in Fig. 5(a). By increasing the sintering temperature to 950 °C, tetragonal phase LLZ along with the minor  $\text{La}_2\text{Zr}_2\text{O}_7$  phase was observed. Raman spectrum of LLZ-0 sintered at 1200 °C indicates that it might be mixture of tetragonal (major) and cubic phase.

Raman spectrum of LLZ-10 sintered at 750 °C revealed the formation of tetragonal phase along with pyrochlore  $\text{La}_2\text{Zr}_2\text{O}_7$  phase. Raman spectrum of LLZ-10 sintered at 950 °C revealed the formation of tetragonal phase whereas the sample sintered at 1200 °C indicated the formation of cubic-like phase. Raman spectra of LLZ-20 sintered at 750 °C and 950 °C revealed the formation of tetragonal phase whereas the sample sintered at 1200 °C indicated the stabilization of cubic-like phase.

Although the Raman spectra (Fig. 5(a) and (b)) of LLZ-0 and LLZ-10 sintered at 1200 °C resemble the high  $\text{Li}^+$  conductive cubic phase a close observation revealed minor change in the Zr-O band position from the 645  $\text{cm}^{-1}$  corresponding to that of high  $\text{Li}^+$  conductive cubic phase. The slight change i.e., shift of 10  $\text{cm}^{-1}$  to higher wave number of Zr-O stretching mode observed in the Raman spectra of LLZ-0 and LLZ-10 sintered at 1200 °C indicated the minor deviation from the high  $\text{Li}^+$  conductive cubic phases LLZ.

The tetragonal phase LLZ is sensitive to humid atmosphere. Hence the LLZ-0 and LLZ-10 sintered at 1200 °C exposed to humid condition during the Raman measurements might be

partially protonated through the  $\text{Li}^+/\text{H}^+$  exchange mechanism and results in to mixture of tetragonal and low temperature cubic phase. The sintering duration of 6 h at 1200 °C might not be sufficient for the inclusion of Al from the alumina crucible in to crystal lattices of LLZ-0, LLZ-10 and LLZ-20 for the stabilization into high  $\text{Li}^+$  conductive cubic phase. The lattice parameter evaluated for the LLZ-10 sintered at 1200 °C was 12.9894(2) Å. The observed slight increase in the lattice parameter compared to that of reported LLZ<sup>2,3</sup> also indicated the possibility of inclusion of proton for lithium in the crystal lattice.

The Raman spectra of Al-LLZ-0, Al-LLZ-10 and Al-LLZ-20 sintered at various temperatures along with the reported patterns of high  $\text{Li}^+$  conductive cubic and tetragonal phase LLZ<sup>21</sup> in the range 50-1200  $\text{cm}^{-1}$  are shown as Figs. 6(a) - (c), respectively. Raman spectra of as-burnt Al-LLZ-0, Al-LLZ-10 and Al-LLZ-20 powders shown as Figs. 6(a) - (c), respectively, also indicated the formation of pyrochlore  $\text{La}_2\text{Zr}_2\text{O}_7$  phase as the first crystallographic phase upon heating as revealed by the PXRD investigation.

The Raman spectrum of Al-LLZ-0 sintered at 750 °C indicated a mixture of  $\text{La}_2\text{Zr}_2\text{O}_7$  and cubic-like phase LLZ as shown in Fig. 6(a). At 950 °C, the Raman spectrum exhibits a minor  $\text{La}_2\text{Zr}_2\text{O}_7$  phase along with the major high  $\text{Li}^+$  conductive cubic ( $Ia\bar{3}d$ ) phase LLZ. The Raman spectrum of Al-LLZ-0 sintered at 1200 °C exhibit characteristic pattern of high  $\text{Li}^+$  conductive cubic ( $Ia\bar{3}d$ ) phase LLZ.

The Raman spectra of Al-LLZ-10 and Al-LLZ-20 sintered at 750 °C indicated a mixture of  $\text{La}_2\text{Zr}_2\text{O}_7$  and cubic-like phase as shown in Figs. 6(b) and (c), respectively. The Raman spectra of Al-LLZ-10 and Al-LLZ-20 sintered at 950 °C revealed the formation of high  $\text{Li}^+$  conductive cubic ( $Ia\bar{3}d$ ) phase. However the presence of Al-O stretching mode at 714  $\text{cm}^{-1}$  indicated the Al containing secondary phases. The Raman spectra of Al-LLZ-10 and Al-LLZ-20 sintered at 1200

°C exhibit characteristic pattern of high Li<sup>+</sup> conductive cubic ( $Ia\bar{3}d$ ) phase without any impurity phase.

The high Li<sup>+</sup> conductive cubic ( $Ia\bar{3}d$ ) phase is found to be formed at relatively lower temperature (950 °C) in the case of Al-LLZ-0 compared to that of the remaining investigated samples, which indicated that the optimized content of Al and Li required for the stabilization of high Li<sup>+</sup> conductive cubic phase may be 0.24 mole and 6.28 mole, respectively as suggested by Rangasamy et al.<sup>17</sup> In the case of Al-LLZ-10 and Al-LLZ-20 the evaporation of excess lithium during the high temperature sintering process accelerated the incorporation of Al in to the crystal lattice. The effect of sintering temperatures and excess lithium source on the phase formation of LLZ and Al-LLZ are shown as Table 1.

### Microstructural analysis

The SEM images of fractured surface of LLZ-0, LLZ-10, LLZ-20, Al-LLZ-0, Al-LLZ-10 and Al-LLZ-20 sintered at 1200 °C are shown as Figs. 7(a) - (f), respectively. The SEM images performed on larger area (50 μm) correspondingly are shown as Figs. S2(a) - (f) in ESI†. The SEM images of fractured surface of LLZ-0 (Figs. 7(a) and S2(a)) indicated that the grains are not in good contact with each other. The SEM images of fractured surface of LLZ-10 (Figs. 7(b) and S2(b)) exhibit slightly better contact with the neighbouring grains along with certain pores when compared to that of LLZ-0. On the other hand, the SEM images of fractured surface of LLZ-20 (Fig. 7(c) and S2(c)) revealed the grains are in more spherical shape and the presence of appreciable amount of pores in between the grains.

The SEM images of fractured surface of Al-LLZ-0 (Figs. 7(d) and S2(d)) exhibit flattened like morphology with certain amount of pores. The SEM image of Al-LLZ-10 (Figs.

7(e) and S2(e)) exhibit more flattened like morphology and was found to be relatively dense compared to that of Al-LLZ-0 and Al-LLZ-20. The SEM image of fractured surface of Al-LLZ-20 (Figs. 7(f) and S2(f)) is transgranular with larger size grains. The Al is known to form an intergranular liquid phase and it may results in significant variations in the grain growth.<sup>26</sup> The addition of excess lithium source and Al doping in LLZ (i.e., Al-LLZ-10) might have led into the formation of possible favorable intergranular Li–Al–O liquid phase at the sintering temperature of 1200 °C. This intergranular Li–Al–O liquid phase could enhance the density of Al-LLZ-10. Fig. S3 in ESI† shows the magnified SEM image of Al-LLZ-20 sintered at 1200 °C. The elemental analysis by EDX (Fig. S3 and Table S1 in ESI†) on Al-LLZ-20 indicated that the Al is more at the grain-boundaries compared to that of at intragrain zones. The excess lithium in Al-LLZ-20 prevents the incorporation of Al in to the crystal lattice hence it may be segregated largely at the grain-boundary. Segregation of secondary phase in the grain-boundary of Al-LLZ-20 might affect the contacts between the grains and it might prevented the formation of flattened like morphology (Figs. 7 (f) and S2 (f)).

The density of the LLZ and Al-LLZ sample sintered at 1200 °C were estimated using Archimedes' principle with deionized water as the immersion medium and the relative density are provided in Table 2. Among all the samples, Al-LLZ prepared with 10 wt % excess lithium source sintered at 1200 °C for just 6 h exhibits a maximized relative density of 95% with particle size of around 613 nm.

### **Impedance analysis**

Typical AC impedance (Cole-Cole) plots of the investigated LLZ and Al-LLZ pellets sintered at 1200 °C measured at room temperature (30 °C) are shown in Figs. 8 and 9, respectively. The AC

impedance plots of LLZ-0, LLZ-10 and LLZ-20 sintered at 1200 °C shown as Figs. 8 (a) - (c), respectively, revealed that the bulk and grain-boundary contribution could not be resolved clearly. Hence, the corresponding room temperature (30 °C) experimental impedance data points of LLZ pellets were fitted with an equivalent circuit shown as inset.

Increasing the amount of lithium source (from 0 wt.% to 20 wt.%) increases the grain boundary resistance which results in to the reduction of total (bulk + grain-boundary)  $\text{Li}^+$  conductivity. Among the investigated LLZ samples, LLZ-0 sintered at 1200 °C exhibited maximized total (bulk + grain-boundary)  $\text{Li}^+$  conductivity of  $8.3 \times 10^{-6} \text{ Scm}^{-1}$  with activation energy of 0.47 eV.

The AC impedance (Cole-Cole) plots fitted with the suitable equivalent circuits (inset) of Al-LLZ-0, Al-LLZ-10 and Al-LLZ-20 pellets sintered at 1200 °C are shown as Figs. 9(a) - (c), respectively. The 20 wt.% excess lithium source in Al-LLZ-20 results into an increase in the grain-boundary resistance which in turn results into decrease in the total (bulk + grain-boundary)  $\text{Li}^+$  conductivity. Excess amount of lithium source may result in the accumulation of unfavorable secondary phase at the grain-boundary, which blocks the  $\text{Li}^+$  migration. The total (bulk + grain-boundary)  $\text{Li}^+$  conductivity was calculated from the inverse of the resistivity derived from the intercepts of the low frequency semicircle (close to the tail) with the real axis. Among the investigated Al-LLZ samples Al-LLZ-10 sintered at 1200 °C exhibited maximized total (bulk + grain-boundary)  $\text{Li}^+$  conductivity of  $5.1 \times 10^{-4} \text{ Scm}^{-1}$  with minimum activation energy of 0.29 eV.

Arrhenius plots for the total (bulk + grain-boundary)  $\text{Li}^+$  conductivity of LLZ and Al-LLZ pellets without excess lithium source (0 wt.%), with 10 wt.% and 20 wt.% excess lithium source sintered at 1200 °C are shown as Fig. S4 in ESI†. The activation energies ( $E_a$ ) for the total (bulk

+ grain-boundary)  $\text{Li}^+$  conductivity were determined from the Arrhenius plots. The lattice parameter, room temperature (30 °C) total (bulk + grain-boundary)  $\text{Li}^+$  conductivity, activation energy (in the temperature range 30 °C to 200 °C) and relative density of LLZ and Al-LLZ pellets sintered at 1200 °C are presented in Table 2. The average diameter for Al-LLZ-10 powder sintered at 1200 °C was found to be 613 nm.

## Conclusions

In this work  $\text{Li}_7\text{La}_3\text{Zr}_2\text{O}_{12}$  (LLZ) and  $\text{Li}_{6.28}\text{Al}_{0.24}\text{La}_3\text{Zr}_2\text{O}_{12}$  (Al-LLZ) were prepared successfully by novel combustion technique and also the consequence of the excess lithium source on the structure,  $\text{Li}^+$  conductivity and morphology of the synthesized materials were examined. The higher  $\text{Li}^+$  conductivity of the Al-containing LLZ should be understood in terms of grain-interior and grain-boundary conduction. The incorporation of  $\text{Al}^{3+}$  at  $\text{Li}^+$  sites enhances the  $\text{Li}^+$  conductivity not only by a transition of the structure from tetragonal to high conductive cubic phase, but also by an increase in  $\text{Li}^+$  vacancies. A further improvement of the total (bulk + grain-boundary)  $\text{Li}^+$  conductivity might be achieved by enhancing the density of the pellets and eliminating the pores through the possible intergranular Li–Al–O liquid phase at the grain-boundary. To derive the high  $\text{Li}^+$  conductive cubic phase LLZ, three factors were considered and optimized: amount of excess lithium, the synthesis temperature and the sintering time. Among all the samples, Al-LLZ prepared with 10 wt.% excess lithium source (Al-LLZ-10) sintered at 1200 °C for just 6 h exhibits maximized relative density of 95% and total (bulk + grain-boundary)  $\text{Li}^+$  conductivity of  $5.1 \times 10^{-4} \text{Scm}^{-1}$  at 30 °C with particle size of around 613 nm. Further fine tuning of sintering temperature and duration of sintering may help to improve the density and  $\text{Li}^+$  conductivity of Al-LLZ-10 further.

The present investigation indicated that this solution combustion process may be a suitable technique for the rapid synthesis of large volume of high  $\text{Li}^+$  conductive cubic phase Al-LLZ with uniform particle size at the nanometer level for industrial production of solid electrolyte for the fabrication of all-solid-state lithium rechargeable and Li-air battery.

† Electronic Supplementary Information (ESI) available: [Additional figures and table mentioned in the text is included here]. See DOI: 10.1039/x0xx00000x

### **Acknowledgements**

The authors thank BRNS, DAE, Mumbai, India [No. 37(3)/14/42/2014-BRNS] for the financial support. RM express his thanks to UGC, New Delhi for the Research Award [F. 30-1/2014/RA-2014-16-OB-PON-5394 (SA-II)].

## References

- 1 G. Girishkumar, B. McCloskey, A. C. Luntz, S. Swanson and W. Wilcke, *J. Phys. Chem. Lett.*, 2010, **1**, 2193.
- 2 R. Murugan, V. Thangadurai and W. Weppner, *Angew. Chem., Int. Ed.*, 2007, **46**, 7778.
- 3 R. Murugan, V. Thangadurai and W. Weppner, *Angew. Chem.*, 2007, **119**, 7925.
- 4 S. Kumazaki, Y. Iriyama, K. H. Kim, R. Murugan, K. Tanabe, K. Yamamoto, T. Hirayama and Z. Ogumi, *Electrochem. Commun.*, 2011, **13**, 509.
- 5 M. Kotobuki, K. Kanamuraa, Y. Sato and T. Yoshid, *J. Power Sources*, 2011, **196**, 7750.
- 6 M. Kotobuki, H. Munakata, K. Kanamura, Y. Sato and T. Yoshida, *J. Electrochem. Soc.*, 2010, **157**, A1076.
- 7 Y. Shimonishi, A. Toda, T. Zhang, A. Hirano, N. Imanishi, O. Yamamoto and Y. Takeda, *Solid State Ionics*, 2011, **183**, 48.
- 8 J. Awaka, N. Kijima, H. Hayakawa and J. Akimoto, *J. Solid State Chem.*, 2009, **182**, 2046.
- 9 M. Huang, T. Liu, Y. Deng, H. Geng, Y. Shen, Y. Lin and C-W Nan, *Solid State Ionics*, 2011, **204**, 41.
- 10 G. Larraz, A. Orera and M. L. Sanjuan, *J. Mater. Chem. A.*, 2013, **1**, 11419.
- 11 N. Janani, S. Ramakumar, L. Dhivya, C. Deviannapoorani, K. Saranya, R. Murugan, *Ionics*, 2011, **17**, 575.
- 12 Y. Jin and P. J. McGinn, *J. Power Sources*, 2011, **196**, 8683.
- 13 R. Djenadic, M. Botros, C. Benel, O. Clemens, S. Indris, A. Choudhary, T. Bergfeldt and H. Hahn, *Solid State Ionics*, 2014, **263**, 49.

- 14 H. Katsui and T. Goto, *Thin Solid Film*, 2015, **584**, 130.
- 15 C. A. Geiger, E. Alekseev, B. Lazic, M. Fisch, T. Armbruster, R. Langner, M. Fechtelkord, N. Kim, T. Pettke and W. Weppner, *Inorg. Chem.*, 2011, **50**, 1089.
- 16 H. Buschmann, J. Dolle, S. Berendts, A. Kuhn, P. Bottke, M. Wilkening, P. Heitjans, A. Senyshyn, H. Ehrenberg, A. Lotnyk, V. Duppel, L. Kienle and J. Janek, *Phys. Chem. Chem. Phys.*, 2011, **13**, 19378.
- 17 E. Rangasamy, J. Wolfenstine and J. Sakamoto, *Solid State Ionics*, 2012, **206**, 28.
- 18 C. Deviannapoorani, L. Dhivya, S. Ramakumar and R. Murugan, *J. Sol Gel Sci. Technol.*, 2012, **64**, 510.
- 19 I. Kokal, M. Somer, P. H. L. Notten and H.T. Hintzen, *Solid State Ionics*, 2011, **185**, 42.
- 20 N. Janani, C. Deviannapoorani, L. Dhivya and R. Murugan, *RSC Adv.*, 2014, **4**, 51228.
- 21 L. Dhivya and R. Murugan, *Appl. Mater. Interfaces (ACS)*, 2014, **6**, 17606.
- 22 C. Galven, J. Dittmer, E. Suard, F. Le Berre, and M. P. Crosnier-Lopez, *Chem. Mater.*, 2012, **24**, 3335.
- 23 H. Xie, Y. Li and J. B. Goodenough, *Mater. Res. Bull.*, 2012, **47**, 1229.
- 24 C. Julien, *Ionics.*, 2000, **6**, 30.
- 25 C. M. Julien and M. Massot, *Mater. Sci. Eng. B.*, 2003, **100**, 69.
- 26 J. H. Ahn, S. Y. Park, J. M. Lee, Y. Park and J. H. Lee, *J. Power Sources*, 2014, **254**, 287.

**Table 1** Effect of sintering temperatures and excess lithium source on the phase formation of LLZ and Al-LLZ.

| Compound   | Sintering Temperature | *Phase Derived   |
|------------|-----------------------|--|
| LLZ-0      | As-burnt              | LZ (major phase) + La <sub>2</sub> O <sub>3</sub> (minor phase)  |
|            | 750 °C                | mixed phase; t-LLZ + LZ  |
|            | 950 °C                | t-LLZ (major phase) + LZ (minor phase)   |
|            | 1200 °C               | mixed phase; t-LLZ + cubic like phase  |
| LLZ-10     | As-burnt              | LZ (major phase) + La <sub>2</sub> O <sub>3</sub> (minor phase)  |
|            | 750 °C                | mixed phase; t-LLZ + LZ  |
|            | 950 °C                | single phase t-LLZ   |
|            | 1200 °C               | cubic like LLZ   |
| LLZ-20     | As-burnt              | LZ (major phase) + La <sub>2</sub> O <sub>3</sub> (minor phase)  |
|            | 750 °C                | t-LLZ  |
|            | 950 °C                | t-LLZ (major phase) + Li <sub>4</sub> ZrO <sub>4</sub> (minor sec. phase)  |
|            | 1200 °C               | cubic like LLZ + La <sub>2</sub> O <sub>3</sub> (minor phase)  |
| Al-LLZ-0   | As-burnt              | LZ (major phase) + La <sub>2</sub> O <sub>3</sub> (minor phase)  |
|            | 750 °C                | mixed phase; cubic like LLZ + LZ + LaAlO <sub>3</sub>  |
|            | 950 °C                | c-LLZ  |
|            | 1200 °C               | single phase c-LLZ   |
| Al-LLZ -10 | As-burnt              | LZ (major phase) + La <sub>2</sub> O <sub>3</sub> (minor phase)  |
|            | 750 °C                | mixed phase; cubic like LLZ + LZ + LaAlO <sub>3</sub>  |
|            | 950 °C                | c-LLZ (major phase) + La <sub>2</sub> Li <sub>0.5</sub> Al <sub>0.5</sub> O <sub>4</sub> (very minor impurity phase) |
|            | 1200 °C               | single phase c-LLZ   |
| Al-LLZ-20  | As-burnt              | LZ (major phase) + La <sub>2</sub> O <sub>3</sub> (minor phase)  |
|            | 750 °C                | mixed phase; cubic like LLZ + LZ + LaAlO <sub>3</sub>  |
|            | 950 °C                | c-LLZ (major phase) + La <sub>2</sub> Li <sub>0.5</sub> Al <sub>0.5</sub> O <sub>4</sub> (minor impurity phase)      |
|            | 1200 °C               | c-LLZ  |

\*LZ: La<sub>2</sub>Zr<sub>2</sub>O<sub>7</sub>; t-LLZ: tetragonal LLZ (*I4<sub>1</sub>/acd*); c-LLZ: high Li<sup>+</sup> conductive cubic LLZ (*Ia $\bar{3}d$* )

**Table 2** Lattice parameter, room temperature (30 °C) total (bulk + grain-boundary) Li<sup>+</sup> conductivity, activation energy (in the temperature range 30 °C to 200 °C) and relative density of LLZ and Al-LLZ pellets without excess lithium source, with 10 wt.% and 20 wt.% excess lithium source sintered at 1200 °C.

| Compound   | Lattice parameter<br>a (Å) | $\sigma_{\text{total}}$<br>30 °C<br>(Scm <sup>-1</sup> ) | E <sub>a</sub><br>(eV) | Relative density<br>(%) |
|------------|----------------------------|--|------------------------|-------------------------|
| LLZ-0      | *-                         | 8.3 x 10 <sup>-6</sup>                                   | 0.47                   | 77                      |
| LLZ-10     | 12.9894(2)                 | 5.1 x 10 <sup>-6</sup>                                   | 0.57                   | 82                      |
| LLZ-20     | 12.9738(3)                 | 2.3 x 10 <sup>-6</sup>                                   | 0.58                   | 83                      |
| Al-LLZ-0   | 12.9757(1)                 | 3.8 x 10 <sup>-4</sup>                                   | 0.43                   | 90                      |
| Al-LLZ -10 | 12.9767(1)                 | 5.1 x 10 <sup>-4</sup>                                   | 0.29                   | 95                      |
| Al-LLZ-20  | 12.9733(2)                 | 5.4 x 10 <sup>-5</sup>                                   | 0.48                   | 88                      |

\* Mixture of tetragonal and cubic-like phase LLZ.

**Figure captions**

**Fig. 1** (a) TG and (b) DSC curves of as-burnt LLZ-0, LLZ-10, LLZ-20, Al-LLZ-0, Al-LLZ-10 and Al-LLZ-20 powders.

**Fig. 2** PXRD patterns of (a) LLZ-0, (b) LLZ-10 and (c) LLZ-20 of as-burnt powder, sintered at 750 °C, 950 °C and 1200 °C along with the reported patterns of cubic ( $Ia\bar{3}d$ ) phase LLZ and tetragonal ( $I4_1/acd$ ) phase LLZ<sup>21</sup> (Impurity phase; \*:  $\text{La}_2\text{Zr}_2\text{O}_7$ , o:  $\text{La}_2\text{O}_3$  and + :  $\text{Li}_4\text{ZrO}_4$ ).

**Fig. 3** PXRD patterns of (a) Al-LLZ-0, (b) Al-LLZ-10 and (c) Al-LLZ-20 of as-burnt powder, sintered at 750 °C, 950 °C and 1200 °C along with the reported patterns of cubic ( $Ia\bar{3}d$ ) phase LLZ and tetragonal ( $I4_1/acd$ ) phase LLZ<sup>21</sup> (Impurity phase; \*:  $\text{La}_2\text{Zr}_2\text{O}_7$ , o:  $\text{La}_2\text{O}_3$ , #:  $\text{La}_2\text{Li}_{0.5}\text{Al}_{0.5}\text{O}_4$  and x :  $\text{LaAlO}_3$ ).

**Fig. 4** Raman spectra of (a) Tetragonal ( $I4_1/acd$ ) phase LLZ (b) High  $\text{Li}^+$  conductive cubic ( $Ia\bar{3}d$ ) phase LLZ (c) Low temperature cubic phase LLZ.<sup>20, 21</sup>

**Fig. 5** Raman spectra of (a) LLZ-0, (b) LLZ-10 and (c) LLZ-20 of as-burnt powder, sintered at 750 °C, 950 °C and 1200 °C along with the reported patterns of cubic ( $Ia\bar{3}d$ ) phase LLZ and tetragonal ( $I4_1/acd$ ) phase LLZ in the range 50-1200  $\text{cm}^{-1}$ .<sup>21</sup>

**Fig. 6** Raman spectra of (a) Al-LLZ-0, (b) Al-LLZ-10 and (c) Al-LLZ-20 of as-burnt powder, sintered at 750 °C, 950 °C and 1200 °C along with the reported patterns of cubic ( $Ia\bar{3}d$ ) phase LLZ and tetragonal ( $I4_1/acd$ ) phase LLZ in the range 50-1200  $\text{cm}^{-1}$ .<sup>21</sup>

**Fig. 7** SEM images of the fractured surfaces of (a) LLZ-0, (b) LLZ-10 and (c) LLZ-20 (d) Al-LLZ-0, (e) Al-LLZ-10, (f) Al-LLZ-20 sintered at 1200 °C for 6 h.

**Fig. 8** Typical room temperature (30 °C) AC impedance (Cole-Cole) plots of (a) LLZ-0, (b) LLZ-10 and (c) LLZ-20 pellets sintered at 1200 °C using Li<sup>+</sup> blocking Au electrodes. Open circle are the experimental data and the solid line represents the fitted data with an equivalent circuit consisting of parallel combination of resistances (R) and constant phase elements (CPEs) representing the electrical bulk, grain-boundary and electrode response, respectively, (R<sub>b</sub>CPE<sub>b</sub>) (R<sub>gb</sub>CPE<sub>gb</sub>) (CPE<sub>el</sub>) (where the subscript b, gb and el refers to the bulk, grain-boundary and electrode contribution, respectively). The fitting curve shown as inset illustrates the separation of bulk and grain-boundary contributions, respectively.

**Fig. 9** Typical room temperature (30 °C) AC impedance (Cole-Cole) plots of (a) Al-LLZ-0, (b) Al-LLZ-10 and (c) Al-LLZ-20 pellet sintered at 1200 °C using Li<sup>+</sup> blocking Au electrodes and the equivalent circuit shown as inset. Open circle are the experimental data and the solid line represents the fitted data with an equivalent circuit using individual resistance and constant phase element (CPE) representing the total contribution from bulk and grain-boundary and electrode response, respectively, (RCPE) (CPE<sub>el</sub>).

## Figures

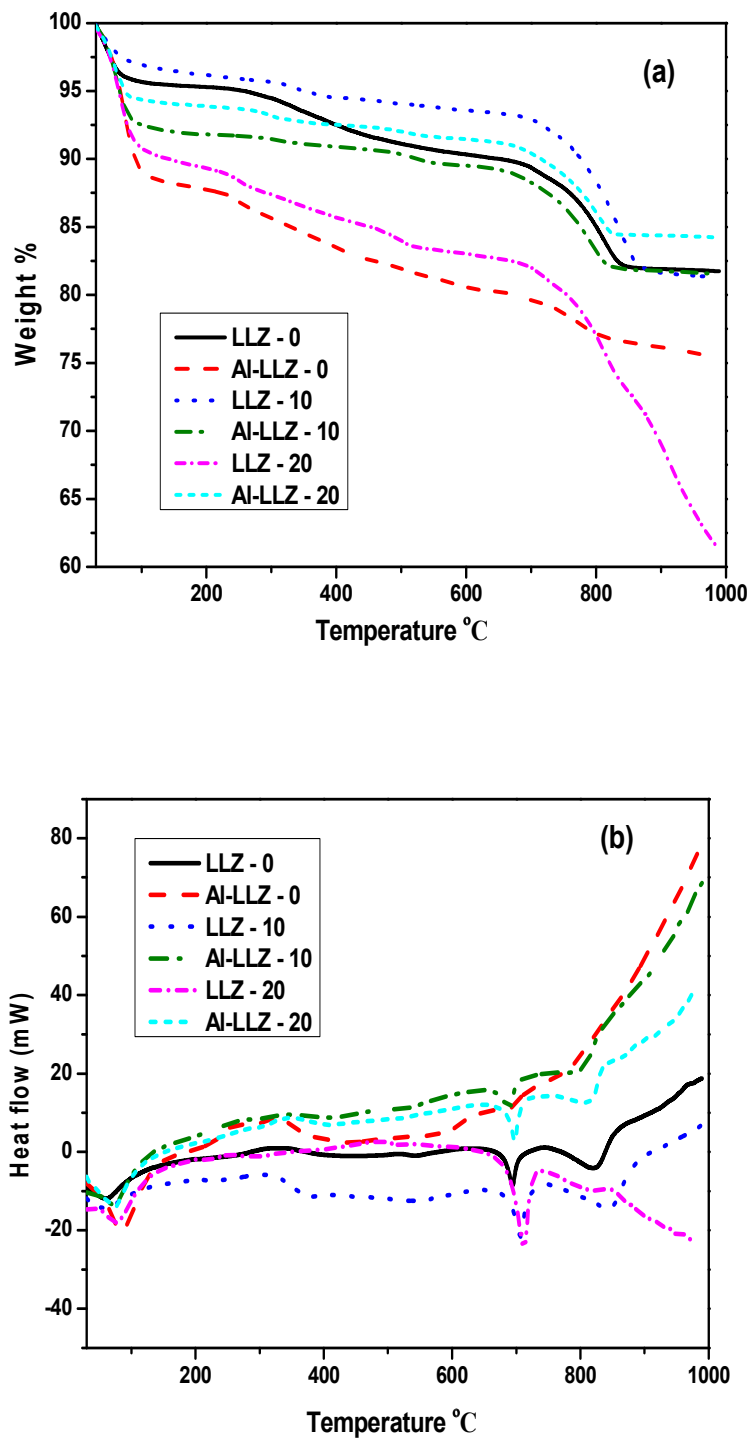


Fig. 1

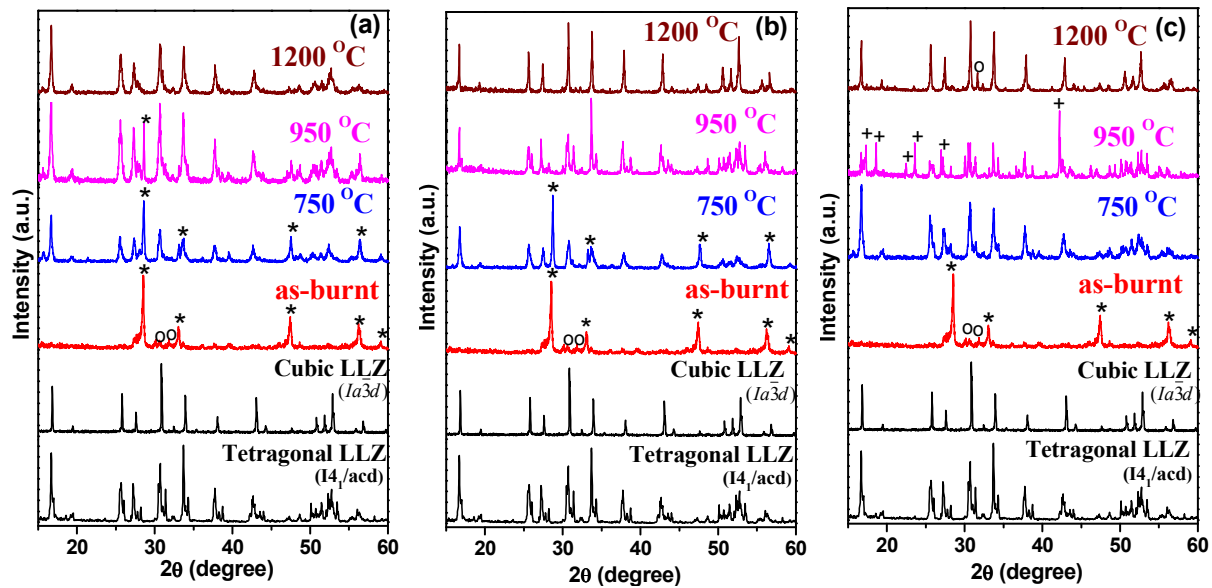


Fig. 2

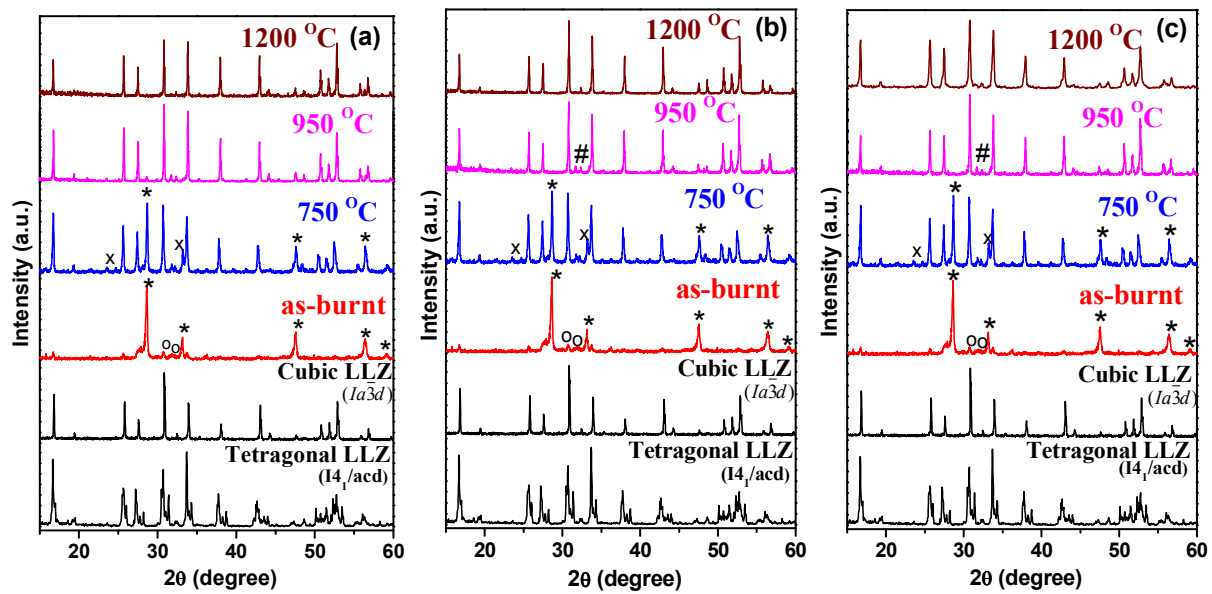


Fig. 3

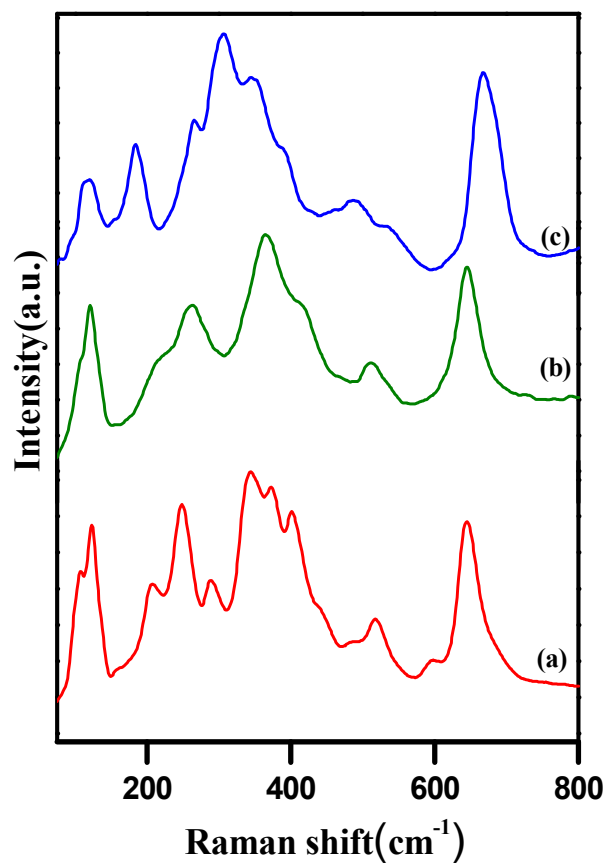


Fig. 4

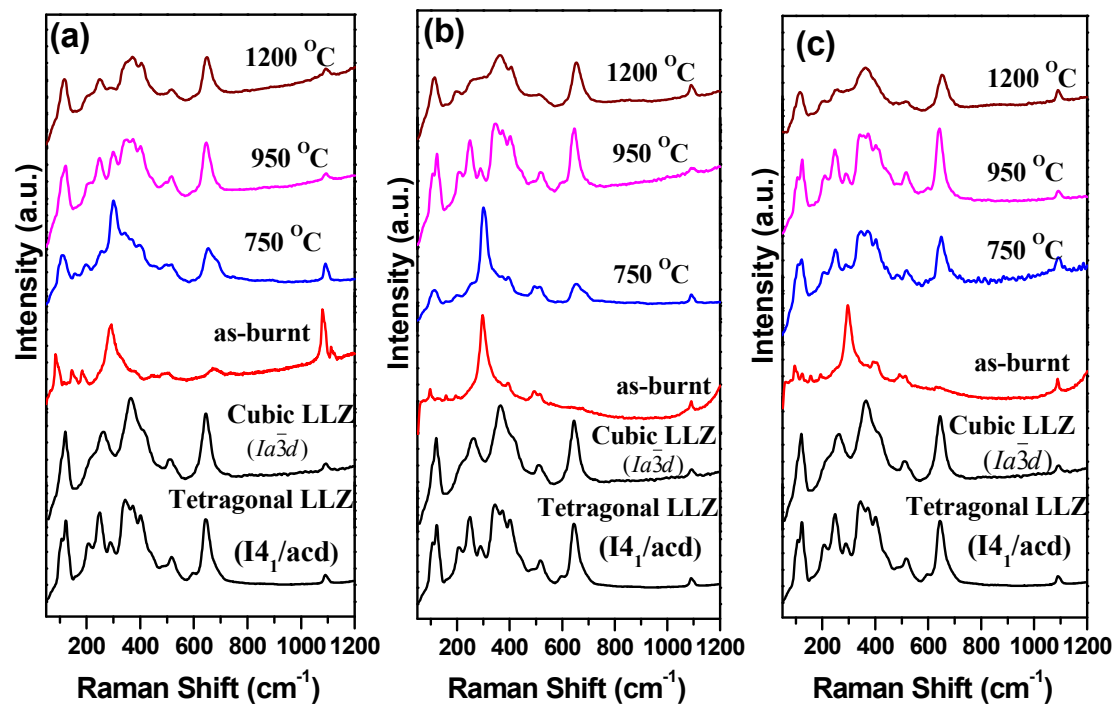


Fig. 5

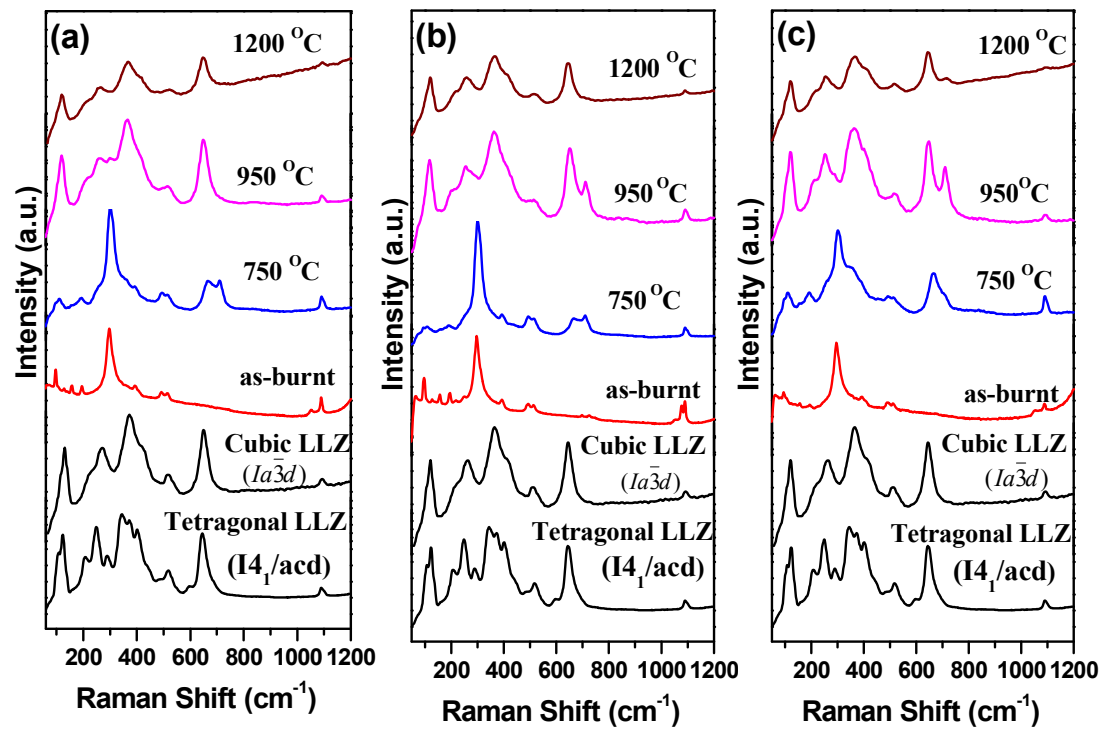
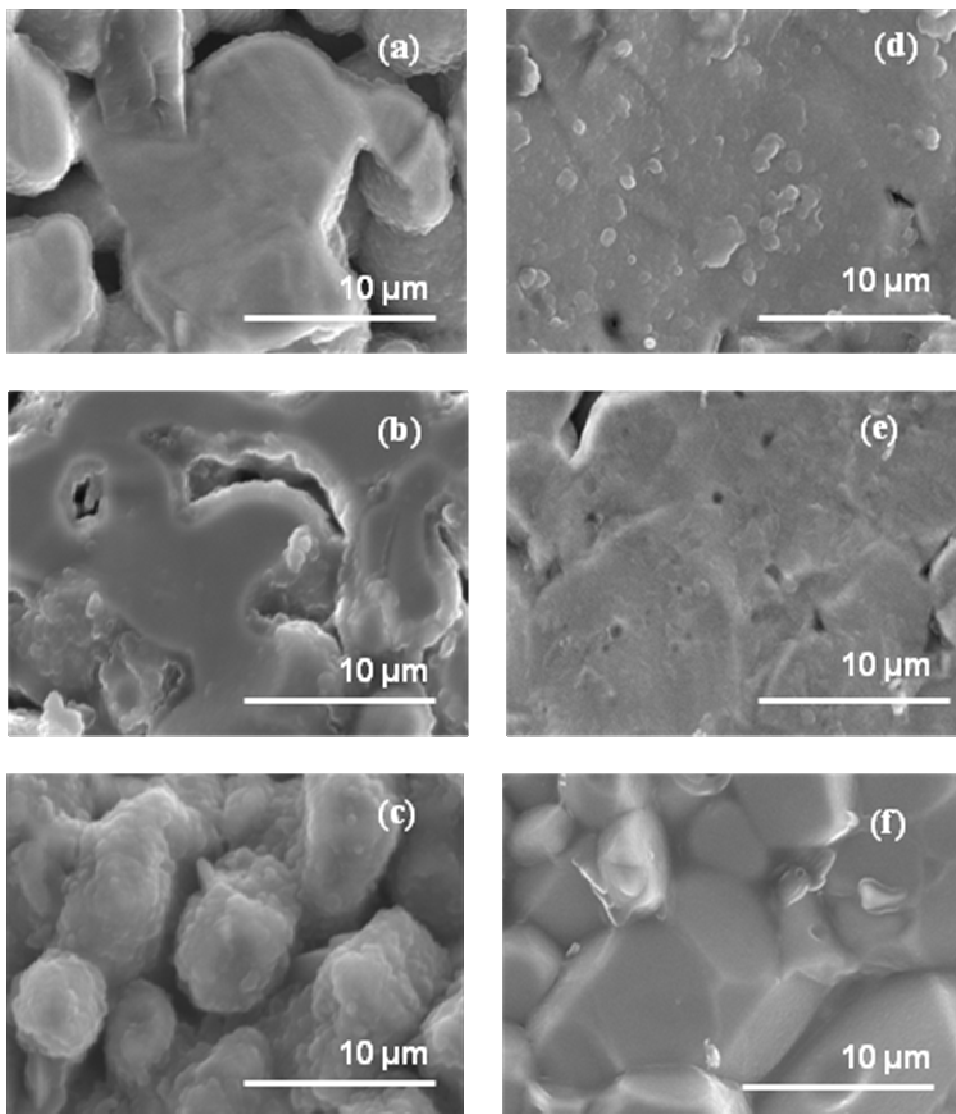


Fig. 6



**Fig. 7**

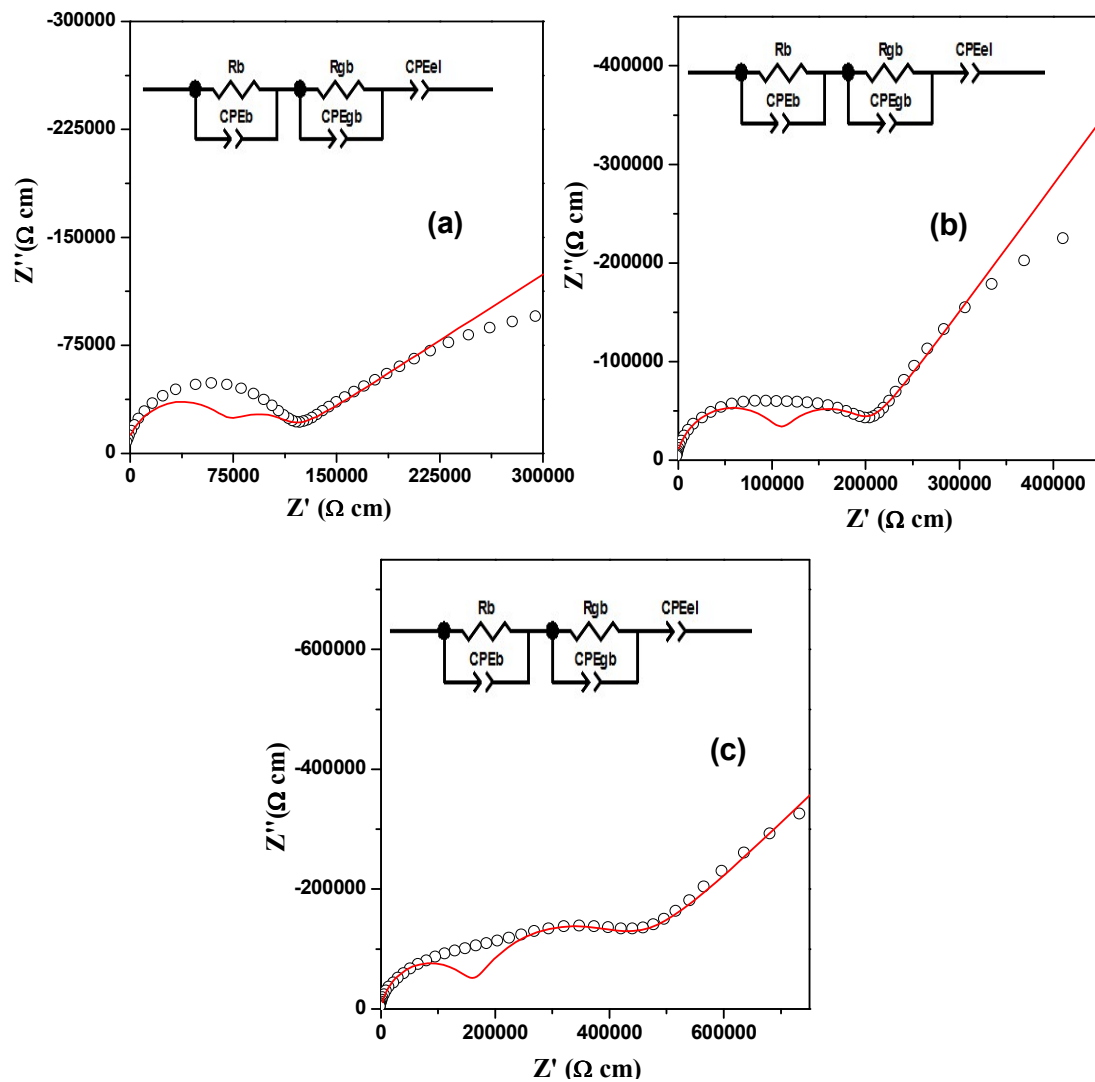


Fig. 8

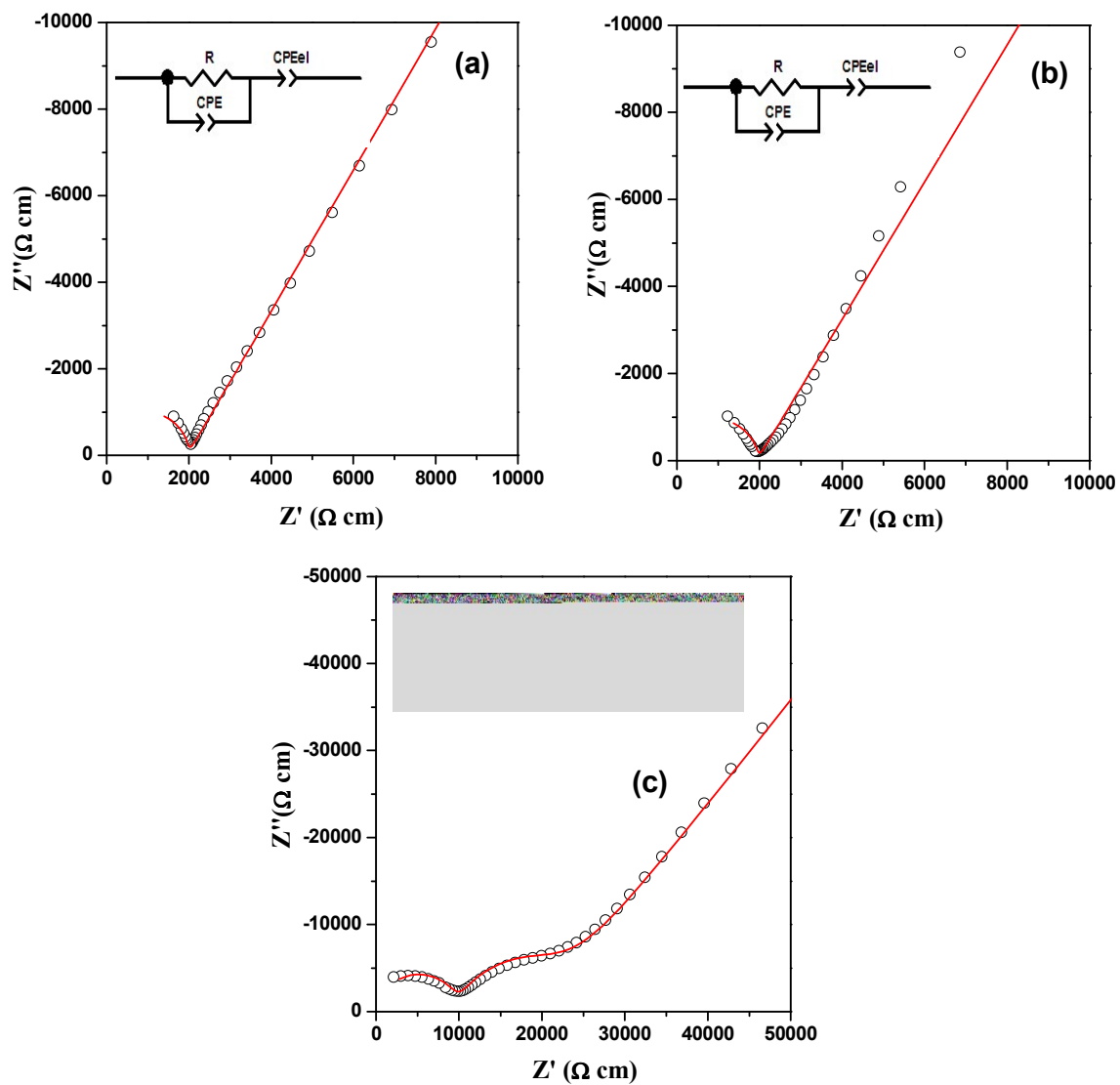


Fig. 9